

HOSTED BY



ELSEVIER

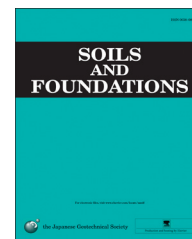


CrossMark

The Japanese Geotechnical Society

Soils and Foundations

www.sciencedirect.com
journal homepage: www.elsevier.com/locate/sandf



On the Role of Geogrid Reinforcement in Reducing Earth Pressure on Buried Pipes: Experimental and Numerical Investigations

M.R. Ahmed, V.D.H. Tran, M.A. Meguid*

Civil Engineering and Applied Mechanics, McGill University, Montreal, Canada

Received 1 June 2014; received in revised form 2 January 2015; accepted 2 February 2015

Available online 16 May 2015

Abstract

Understanding the distribution of earth pressure on buried structures is essential for the analysis and design of pipes, tunnels and vertical shafts. This paper presents the results of an experimental investigation that has been conducted to measure the distribution of contact pressure on rigid pipes using tactile sensing technology. The method allows for a continuous pressure profile to be measured around the pipes using flexible sheets that can follow the cylindrical shape of the pipes. The physical model involves a buried pipe installed in granular material subjected to strip surface loading. The effect of introducing a geogrid reinforcement layer above the pipe on the distribution of contact pressure is also examined. To further study the distribution of pressure on the buried structure and the soil-geogrid interaction, numerical analyses are performed using a multi-scale finite-discrete element framework that allows for both the explicit modeling of soil particles using discrete elements and the modeling of the embedded structure using finite elements. The numerical framework is first validated using the experimental results and then used to investigate the detailed behavior of the soil-pipe system.

© 2015 The Japanese Geotechnical Society. Production and hosting by Elsevier B.V. All rights reserved.

Keywords: Contact pressure measurement; Buried pipes; Multi-scale modeling; Finite-discrete element

1. Introduction

Measuring the earth pressure acting on buried structures has been used in practice to monitor the performance of subsurface structures including foundations, culverts, buried pipes, retaining walls and tunnel linings. Pneumatic, hydraulic, vibrating wire and strain-gauge based devices are among the commonly used techniques for earth pressure measurement, particularly for large-scale projects where stiff load cells are installed at

selected locations against the walls of the structure. The performance of different contact pressure measurement cells in geotechnical engineering applications has been reported by several researchers, including Carlson (1939), Peattie and Sparrow (1954), Selig (1964), Hanna (1985), Dunncliff and Green (1988), Lazebnik and Tsinker (1997), Talesnick (2005), Ahmed and Meguid (2009) and Corey et al. (2014). It has been concluded that rigid cells typically read stress levels that are either low or high relative to the actual soil stress depending on the cell stiffness, size, aspect ratio and placement procedures (Selig, 1964; Kohl et al., 1989; Talesnick et al., 2011).

Tactile pressure sensors, adapted from the robotics industry, have been successfully used in geotechnical engineering applications to measure the distribution of normal stress in granular soils (Paikowsky and Hajduk, 1997; Paikowsky et al., 2000, 2002, 2006; Springman et al., 2002). A standard tactile

*Correspondence to: Civil Engineering and Applied Mechanics, McGill University, 817 Sherbrooke St. W. Montreal, Quebec, Canada H3A 0C3. Tel.: + (514) 398 1537; fax: + (514) 398 7361.

E-mail addresses: mahmoud.ahmed@mail.mcgill.ca (M.R. Ahmed), viet.tran@mail.mcgill.ca (V.D.H. Tran), mohamed.meguid@mcgill.ca (M.A. Meguid).

Peer review under responsibility of The Japanese Geotechnical Society.

sensor typically consists of an array of force-sensitive cells embedded between two flexible polymeric sheets to measure the normal pressure distribution. Due to their limited thickness (usually less than 1 mm), tactile sensors possess favourable characteristics with respect to the aspect ratio and the stiffness over conventional load cells. In addition, being flexible enables the shaping of the sensing pads to cover curved surfaces. Hence, they are suitable for cylindrically shaped structures (e.g., pipes, shafts or tunnels). Palmer et al. (2009) used tactile sensing technology to measure the contact pressure on a buried pipe subject to lateral loading, considering the time-dependent characteristics of the polymeric sheet containing the sensing units. Tessari et al. (2010) reported that tactile pressure sensors can be used in geotechnical centrifuge to measure at-rest, active and passive lateral earth pressure values on retaining structures. Olson et al. (2011) used tactile sensors to record the seismic earth pressure acting on model foundations in a series of centrifuge tests. Gillis (2013) developed a calibration method for tactile pressure sensors to be used in geotechnical centrifuge. Ahmed et al. (2013) used tactile (TactArray) sensors to measure the distribution of contact pressure on a buried structure subjected to repeated loading. The sensors consist of two specially designed pads containing two sets of orthogonal electrodes (plates) separated by a flexible insulator that acts as a spring allowing for conformable and stretchable pad designs. The tactile pads have proven to provide high sensitivity and repeatability of the measured pressure. Enhancing the bearing capacity of shallow foundations using geogrid reinforcement has recently been investigated by several researchers (e.g., Abu-Farsakh et al., 2013; Chakraborty and Kumar, 2014). Corey et al. (2014) presented the laboratory results of a high-density polyethylene pipe buried at a shallow depth and subjected to static loads with or without geogrid. The contact pressure and the deflection of the flexible pipe were recorded as the results of the geogrid reinforcement.

In this study, an investigation into the distribution of contact pressure on buried pipes is conducted using both experimental and numerical methods. The experimental work involves a thick-walled PVC pipe that is instrumented with tactile sensors and buried in granular material, while a vertical strip load is applied at the surface above the centreline of the pipe. The effect of placing a geogrid reinforcement layer on the distribution of radial earth pressure is examined. Validated by the experimental results, a multi-scale numerical model is then developed and used to investigate the earth pressure on the pipe over a range of applied loading. In this technique, the three-dimensional geometries of the geogrid and the pipe are properly modeled using finite elements (FE), while the soil particles are modeled using discrete elements (DE). The coupling of the finite and discrete element methods allows for the modeling of the interaction between the pipe and the soil and provides a closer look into the three-dimensional response of the geogrid material.

The experimental setup and test procedure are first presented followed by a brief description of the numerical framework used to carry out the analysis. The results of both the physical and numerical models are then grouped and compared to allow

for the validation of the developed model. The responses of both the pipe and the geogrid layer are investigated under increasing surface loading up to soil failure.

2. Experimental Study

The experimental setup consists of a thick-walled pipe embedded in granular backfill material contained in a strong box. The pipe is instrumented using tactile sensing pads wrapped around its outer perimeter covering the area near the middle third of the pipe length. A universal MTS testing machine with a capacity of 2650 kN is used to apply the strip loading (see Fig. 1). A detailed description of the experimental setup components is given below.

2.1. Strong box

The strong box used in the experiments is shown schematically in Fig. 1a. The box dimensions ($1.4 \text{ m} \times 1.0 \text{ m} \times 0.45 \text{ m}$) are selected such that they represent a two-dimensional loading condition. The rigid walls are placed far from the pipe to minimize the boundary effects. The distance from the outer

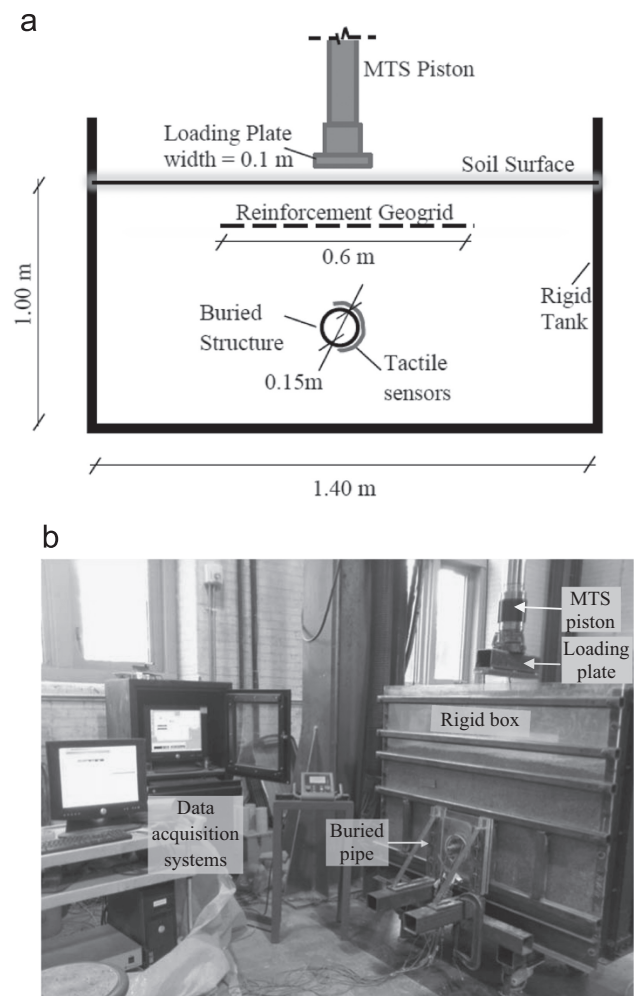


Fig. 1. Testing facility used in experimental work: a) Schematic of rigid tank and buried pipe and b) Photograph showing details of experimental setup.

perimeter of the pipe to the side walls of the tank is 0.65 m, which is more than 4 times the pipe diameter. All the steel wall surfaces are painted with epoxy coating and covered with two plastic sheets - the first is taped directly onto the walls of the box, whereas the second is loosely placed such that the two sheets are separated by a thin layer of grease to minimize friction between the backfill material and the rigid walls during the soil placement and the surface loading process.

2.2. Instrumented pipe

A thick-walled PVC pipe, with an outer diameter of 15 cm and a wall thickness of 1 cm, is used in this study. The pipe crown is placed 0.45 m below the soil surface and instrumented using two custom-made pressure sensing pads installed directly on the pipe. The TactArray distributed pressure measurement system (Pressure Profile Systems, Los Angeles, CA, USA) used in this study consists essentially of two sets of orthogonal electrodes (plates) separated by a flexible insulator that acts as a spring allowing for conformable and stretchable pad designs. When a normal load is applied on the sensors, it changes the distance between the electrodes, resulting in a change in capacitance. Applying a tangential force changes the effective area between the plates. Thus, the capacitive sensors are capable of detecting pressure levels by sensing the applied normal and tangential forces. Each sensing pad contains 255 square-shaped sensors with pressure in the range of 0 to 140 kPa. The sensors are protected from backfill abrasion by covering the instrumented pipe with a thin layer of stiff rubber sheet (1 mm in thickness), as shown in Fig. 2a. Shim stocks, made from the same pipe material, are used to provide a similar contact surface condition to the original pipe and to absorb the shear stress developing at the soil-pipe interface.

It should be noted that, although the pipe has been chosen to perform such that no significant deformation develops during loading, two LVDTs are installed orthogonally inside the pipe to ensure the validity of this assumption. The maximum recorded change in diameter, at a surface pressure of 140 kPa, was found to be less than 0.05 mm which is considered to be insignificant.

2.3. Sensor calibration

In addition to the manufacturer's calibration, further laboratory testing was conducted on the sensing pads placed over both flat and curved surfaces. A setup was designed by fabricating two different wooden frames, the first having rectangular-shaped walls and the second being designed such that the lower end of two opposing walls would be cut with a half-circular profile that fits over the instrumented pipe. The boxes were then filled with gravel of a known weight (2000 g), and the pressure distribution and the total weight were recorded by the data acquisition system connected to the sensors. In both cases, the results showed pressure readings consistent with the applied load.

A series of experiments was also conducted to study the effect of the protective layers on the measured pressure.

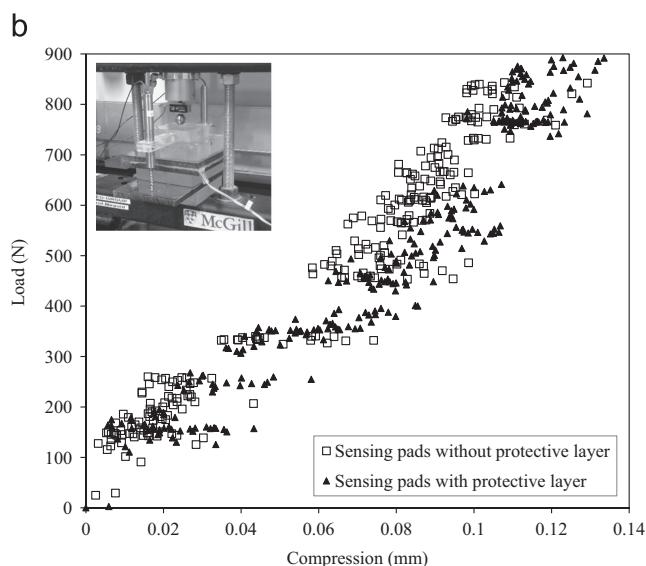
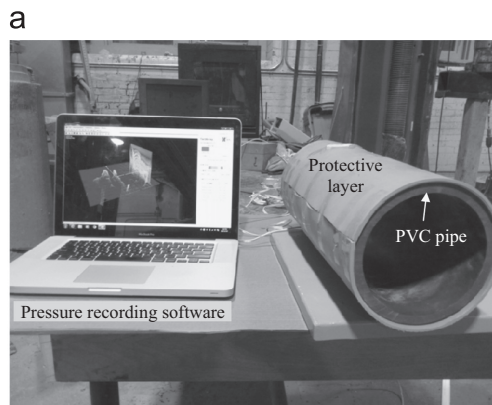


Fig. 2. a) Instrumented pipe and b) effect of protective layers on measured pressure.

A pneumatic system was used to apply vertical pressure directly over the sensing pad. The pressure was gradually increased up to a value comparable to that expected in the experiment. The responses before and after the addition of the protective layers were compared (Fig. 2b). The results show scattered pressure readings recorded by the sensing pad with a compression of about 0.13 mm at an applied load of 900 N. An insignificant increase in compression was recorded after the addition of the protective layer above the sensing pad. This indicates that the chosen protective material is stiff enough and does not cause additional compression under the loading level expected in the experiment.

2.4. Testing procedure

In this study, the soil placement procedure has been used in all tests to ensure consistent initial conditions. A total of four experiments were conducted including two benchmark tests, with only the instrumented pipe inside the backfill, and two with one layer of biaxial geogrid.

Dry sandy gravel, with an average unit weight of 16.3 kN/m³, was used as backfill material. The sieve analysis, conducted

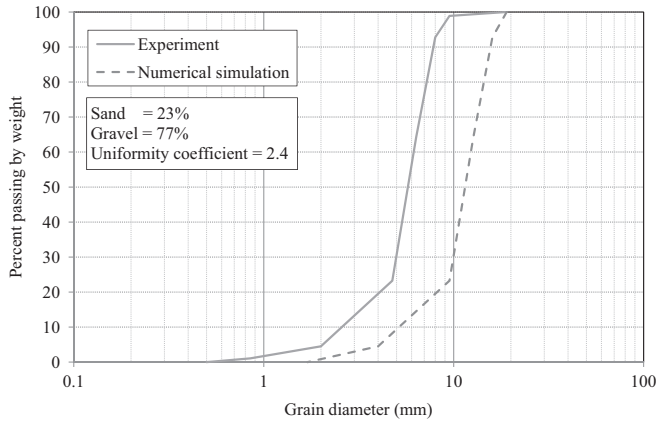


Fig. 3. Particle size distribution of backfill material.

Table 1
Properties of the backfill material.

Property	Value
Specific gravity	2.65
Coefficient of uniformity (C_u)	2.4
Coefficient of curvature (C_c)	1.6
Minimum dry unit weight (γ_{min})	15.1 kN/m ³
Maximum dry unit weight (γ_{max})	17.3 kN/m ³
Experimental unit weight (γ_d)	16.3 kN/m ³
Internal friction angle (ϕ)	47°
Cohesion (c)	0

on selected samples, indicated a coarse-grained material with 77% gravel and 23% sand. The friction angle of the backfill, determined using direct shear tests, is found to be 47°. The grain size distribution of the soil is shown in Fig. 3. The soil was placed and tamped in layers to form a dense base bedding material below the pipe. The instrumented pipe was then placed over a thin sand layer to improve the contact between the soils and the pipe. Backfill placement continued in layers over and around the pipe up to the target soil height of 1.0 m. The density of the backfill was measured in the rigid box using density cups placed at different locations and collected after the completion of the tests. The properties of the backfill material are summarized in Table 1. The placement of the thin sand layer, in contact with the pipe (less than 2% by weight of the bedding layer), was found to cause insignificant changes in soil density or friction angle.

Geogrid type BX1100 (polypropylene material with tensile modulus of 205 kN/m at 2% strain), with dimensions of 0.4 m × 0.6 m, is placed at a depth of 5 cm below the sand surface. For all tests, the placement of the backfill continued up to a distance of 0.45 m above the crown. The radial earth pressure distributions on the pipe were measured using the tactile sensors. Surface load was then applied using a rectangular steel plate (45 cm long × 10 cm wide) attached to the actuator of the MTS machine and placed above the pipe centerline. The load was gradually applied for five minutes under displacement control with a displacement rate of 1.3 mm/min. The test was stopped when either a surface

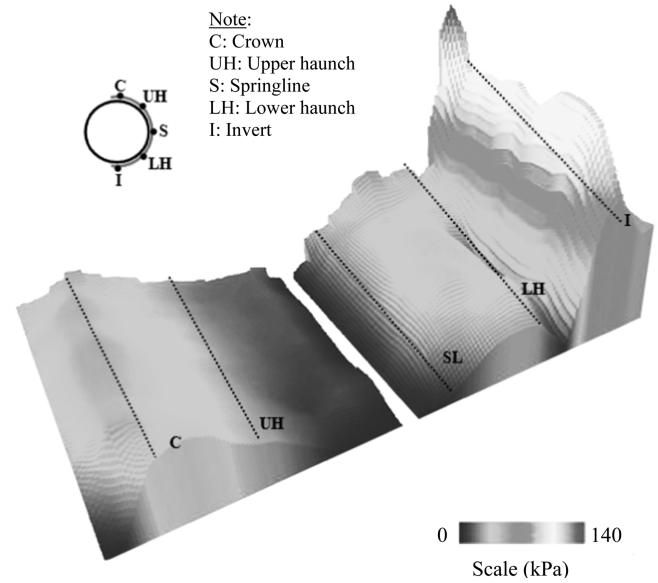


Fig. 4. Snapshot of measured earth pressure distribution around pipe.

displacement of 6.5 mm was reached or the pressure on the tactile sensors exceeded the allowable capacity. After the completion of each test, the tank was emptied using a vacuum machine connected to a collection barrel. The pipe was then retrieved and the setup was prepared for the next test. A sample of the radial pressure distribution, recorded by the data acquisition software, is shown in Fig. 4.

3. Numerical Analysis

3.1. Coupled finite-discrete element framework

The coupled FE-DE framework developed in this study is a continuation of the original work of Dang and Meguid (2010, 2013) and Tran et al. (2013, 2014). The adopted numerical algorithm is briefly described in the following sections.

3.1.1. Finite Elements

The FE analysis in the framework is performed using an explicit dynamic approach. The general equation is expressed as:

$$K\mathbf{x} + C\dot{\mathbf{x}} + M\ddot{\mathbf{x}} = \mathbf{P} \quad (1)$$

where, K is the stiffness matrix, C is the damping matrix, M is the mass matrix, \mathbf{P} is the external force vector and \mathbf{x} represents the displacement vector.

An explicit time integration technique is used to obtain the solution for Eq. (1) utilizing a computationally efficient central-difference scheme. Mass proportional damping is employed to avoid the assembly of the global stiffness matrix. Eq. (1) can then be written as:

$$K\mathbf{x} + cM\dot{\mathbf{x}} + M\ddot{\mathbf{x}} = \mathbf{P} \quad (2)$$

where, c is the damping coefficient.

In order to satisfy the convergence condition, time step Δt_{FE} must be smaller than maximum time step $[\Delta t_{FE}]$ determined by

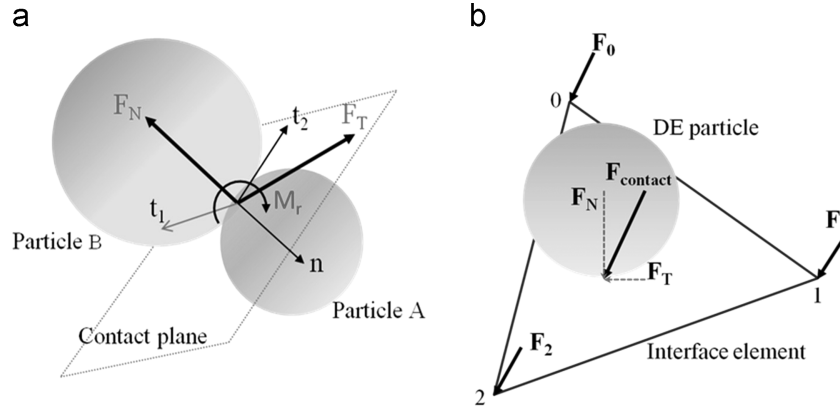


Fig. 5. a) Interaction between two DE particles and b) Forces transmitting to FE nodes through DE particle- interface element interaction.

the maximum eigenvalue:

$$\Delta t_{FE} \leq [\Delta t_{FE}] = \frac{2}{\sqrt{\lambda_m}} \tag{3}$$

where, λ_m is the maximum eigenvalue,

$$\lambda_m \leq \max_i \sum_{j=1}^n \frac{|K_{ij}|}{M_{ii}} \tag{4}$$

3.1.2. Discrete Elements

The discrete element method is used to model the backfill soil as a set of discrete particles interacting with each other in a dynamic process based on a time-stepping algorithm and explicit finite difference scheme. Translational and rotational dynamic motions of the discrete elements are determined using the following equations:

$$\mathbf{F}_i = m(\ddot{\mathbf{x}}_i - \mathbf{g}_i) \tag{5}$$

where, \mathbf{F}_i is the sum of all the external forces acting on particle i , m is the mass of the particle, $\ddot{\mathbf{x}}_i$ is the particle acceleration and \mathbf{g}_i is the body force acceleration vector.

$$\mathbf{M}_i = \dot{\mathbf{H}}_i \tag{6}$$

where, \mathbf{M}_i is the moment acting on the particle and $\dot{\mathbf{H}}_i$ is the particle angular momentum.

The interaction between DE particles is determined using contact laws (Šmilauer and Chareyre, 2010) and the resulting energy is dissipated using damping coefficients, as described below.

The interaction between two particles, A and B (Fig. 5a), is represented by normal force $\vec{\mathbf{F}}_N$, tangential force $\vec{\mathbf{F}}_T$ and rolling resistance moment $\vec{\mathbf{M}}_r$. The normal and tangential contact forces are determined using the normal penetration between the two particles, $\vec{\Delta}_N$, and the incremental tangential displacement, $\delta \vec{\Delta}_T$, such that:

$$\vec{\mathbf{F}}_N = K_N \cdot \vec{\Delta}_N, \delta \vec{\mathbf{F}}_T = -K_T \cdot \delta \vec{\Delta}_T \tag{7a, b}$$

where, K_N and K_T are the normal and the tangential stiffness values, respectively, at contact, defined by:

$$K_N = \frac{2E_A r_A E_B r_B}{E_A r_A + E_B r_B} \tag{8}$$

and

$$K_T = \alpha K_N \tag{9}$$

where, E is the particle material modulus, r is the particle radius and α is a constant ratio.

Rolling resistance moment $\vec{\mathbf{M}}_r$ is introduced to represent the rolling restraint between the two particles. $\vec{\mathbf{M}}_r$ is calculated using rolling angular vector $\vec{\theta}_r$ that describes the change in relative orientation between particles by summing the angular vector of the incremental rolling.

It is noted that both tangential force $\vec{\mathbf{F}}_T$ and moment $\vec{\mathbf{M}}_r$ are limited by a threshold value such that:

$$\vec{\mathbf{F}}_T = \frac{\vec{\mathbf{F}}_T}{\|\vec{\mathbf{F}}_T\|} \|\vec{\mathbf{F}}_N\| \tan(\varphi_{micro}) \text{ if } \|\vec{\mathbf{F}}_T\| \geq \|\vec{\mathbf{F}}_N\| \tan(\varphi_{micro}) \tag{10}$$

and

$$\vec{\mathbf{M}}_r = \begin{cases} K_r \vec{\theta}_r & \text{if } K_r \|\vec{\theta}_r\| < \|\vec{\mathbf{M}}_r\|_{lim} \\ \|\vec{\mathbf{M}}_r\|_{lim} \frac{\vec{\theta}_r}{\|\vec{\theta}_r\|} & \text{if } K_r \|\vec{\theta}_r\| \geq \|\vec{\mathbf{M}}_r\|_{lim} \end{cases} \tag{11}$$

where,

$$\|\vec{\mathbf{M}}_r\|_{lim} = \eta_r \|\vec{\mathbf{F}}_N\| \frac{r_A + r_B}{2} \tag{12}$$

K_r is the rolling stiffness of the interaction; it is calculated using the following equation:

$$K_r = \beta_r \left(\frac{r_A + r_B}{2} \right)^2 K_T \tag{13}$$

where, β_r is the rolling resistance coefficient and η_r is a dimensionless coefficient.

To ensure the stability of the DE model, critical time-step Δt_{cr} is determined:

$$\Delta t_{cr} = \min_i \sqrt{2} \sqrt{\frac{m_i}{K_i}} \tag{14}$$

where, m_i is the mass of particle i and K_i is the per-particle stiffness of the contacts in which particle i participates.

3.1.3. Interface Elements

Interface elements are used to assure the interaction between the FE and DE domains. Triangular facets are used as interface elements and directly defined by the three nodes of the finite element located on the interface (for tetrahedral-shaped elements). If hexahedral elements are used, the contact interface is divided into four triangular facets by creating a temporary center node determined by:

$$x^{(0)} = \frac{1}{4} \sum_{i=1}^4 x^{(i)} \quad (15)$$

where, $x^{(i)}$ is the coordinate of node i of the quadrilateral.

The interaction between a discrete particle and an interface element is illustrated in Fig. 5b using a contact algorithm similar to that used between the DE particles. In each computational step, a set of potential particle-interface contacts is first obtained through spatial sorting. The contact between a DE particle and an interface element is then determined based on the separating distance as well as the projected location of the particle center on the interface element. Normal penetration $\vec{\Delta}_N$ and incremental tangential displacement $\delta \vec{\Delta}_T$ are determined allowing for the normal and tangential contact forces to be calculated. The interaction forces, transmitted to the FE nodes, can then be calculated as follows:

$$\vec{F}_i = \vec{F}_{contact} \cdot N_i \quad (16)$$

where, $\vec{F}_{contact} = \vec{F}_N + \vec{F}_T$ is the total contact force and N_i are the shape functions obtained using the natural coordinates of the contact point.

The contact forces developing on both the DE and FE domains result in DE particle movement and the deformation of the FE structure. This, in turn, leads to the deformation of the interface elements and the generation of new potential particle-interface interactions.

As the time step Δt_{FE} required for FE is much larger than that required for DE (Δt_{DE}), using different time steps for each domain improves the computational efficiency. In this study, the time step used in the FE domain is selected such that $\Delta t_{FE} = n \Delta t_{DE}$ where n is an integer such that $n \leq \frac{[\Delta t_{FE}]}{\Delta t_{DE}}$. This algorithm is implemented by executing the FE solver for every n DE computation step.

A typical FE-DE computational cycle consists of the following main steps:

i) Contact is detected between the DE particles and the interface elements; ii) The interaction parameters of each contact are calculated; iii) The particle-particle and the particle-interface interactions are evaluated; iv) The particle velocities are calculated and their positions are updated. For every n time step, the FE solver is executed and the forces acting on the FE nodes are re-calculated to determine the node displacements. Newly deformed geometries are obtained for both the FE and the interface elements.

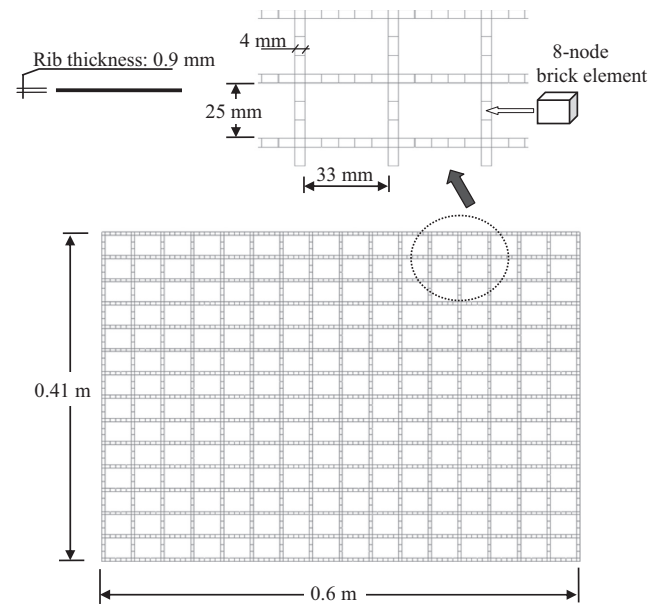


Fig. 6. Plan view of geogrid.

3.2. Modeling details

The geogrid and the pipe are modeled using FE, while the soil is modeled using DE, as discussed in the previous sections. Interface elements are used to simulate the interaction between the two domains. The biaxial geogrid, which comprises 15 longitudinal elements and 17 transverse elements, is modeled using 8-node brick elements (Fig. 6). It is noted that the local increase in geogrid joint thickness is not considered in the model in order to simplify the numerical analysis. A linear elastic model is used for the geogrid material. The Young's modulus of the geogrid (BX1100) is determined by matching the calculated tensile test results with those measured in the index test at a strain of 2% ($E = 1.4 \times 10^3$ MPa), as summarized in Table 2. This assumption is considered appropriate since the observed geogrid deformation is rather small. The full geometry of the geogrid, which comprises over 2100 finite elements and 15,000 interface elements, is shown in Fig. 6. The number of finite elements is chosen to ensure reasonable accuracy and, at the same time, to keep the computational costs at an acceptable level. The geogrid elements are fully covered by interface elements; and therefore, the soil-geogrid interaction at all contact points within the model is properly simulated. In addition, particles on either side of the geogrid are allowed to move freely through the geogrid apertures. They interact with other particles in a similar manner to that experienced in pullout experiments.

The pipe is modeled using shell elements with material properties based on those measured in the laboratory, as shown in Table 2. Since the deformation of the pipe measured in the experiments was found to be negligible, the elastic model is deemed sufficient for the pipe material.

The backfill used in the experiment is modeled using spherical particles. The simplified particle shape greatly improves the computational efficiency as it minimizes the

Table 2
Input parameters used in the numerical analysis.

Type of elements	Parameter	Value
Discrete particles	Density (kg/m^3)	2700
	Material modulus E (MPa)	100
	Ratio K_T/K_N	0.25
	Coefficient of friction ($\tan \varphi_{micro}$)	0.87
	β_r	0.02
	η_r	1.0
	Damping coefficient	0.2
8-node brick elements (for geogrid simulation)	Young's modulus E (MPa)	1.4E+3
	Poisson's ratio ν	0.45
Shell elements (for pipe simulation)	Young's modulus E (MPa)	2.8E+3
	Poisson's ratio ν	0.38
Interface elements	Material modulus E (MPa)	100
	Ratio K_T/K_N	0.25
	Coefficient of friction ($\tan \phi$)	0.45

need to bond much smaller spheres to create the shape of the gravel particle.

Although the predefined particle size distribution has a significant effect on the behavior of the discrete element system, it is numerically prohibitive to simulate millions of particles with their actual sizes. Therefore, particle up-scaling is necessary to reduce the number of modeled particles and to increase the critical time step of the simulation. Consideration is usually given to particle size in order to maintain a balance between computational costs and the scaling effects on the sample response. A small-scale factor (ratio between the sizes of the spheres and real particles) of 2 is chosen in this study (see Fig. 3). According to Potyondy and Cundall (2004), when the number of particles is large enough (over 300,000 particles in this analysis with a scale factor of 2), the macroscopic response becomes independent of the particle sizes.

The thin sand layer used to improve the contact between the soils and the pipe is modeled using spherical particles following a normal distribution with a mean diameter of 6 mm and a standard deviation of 1.2 mm. Soil particles are generated in this study using the gravitational approach proposed by Tran et al. (2013) to represent the backfill placement in layers under gravity, as summarized below.

Layers of particles (about 0.05 m in thickness) are generated to form the backfill material. To build the first layer, a set of non-contacting particles is generated until the target volume is reached. This target volume is calculated based on the porosity of the sand, which is given to be 0.41. The initial height of the box is chosen to be larger than the target height of the layer to ensure that all particles can be generated without overlapping. Gravity is then applied to all particles allowing them to move downward and to come into contact with each other. The inter-particle friction angle is initially set to zero. Lateral shaking is applied to the box to help small particles move into the voids located between larger particles. The geogrid and the pipe are generated during the packing process to ensure the proper interaction with the DE particles. Particles at the locations of the geogrid and the pipe are removed, and the geogrid, the pipe and the interface elements are generated. The next cloud of

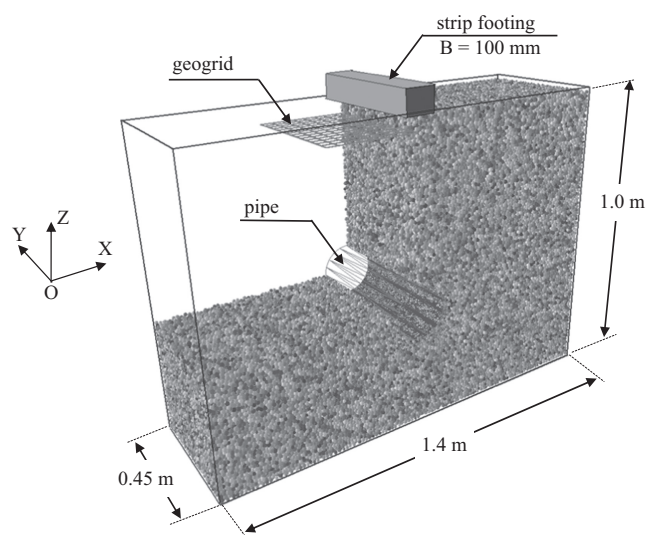


Fig. 7. Partial view of numerical model showing geogrid layer and buried pipe.

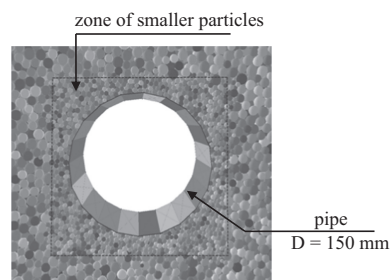


Fig. 8. Close view of pipe and surrounding particles.

particles is generated and the procedure is repeated until the final backfill volume is formed. The 3D geometry of the final sample, with over 300,000 particles, is shown in Fig. 7. A close view of the pipe model and its surrounding DE particles is shown in Fig. 8.

The parameters needed for the discrete element analysis are determined by matching the numerical and the experimental

direct shear test results. The box has dimensions of 101.6 mm × 101.6 mm. During the shearing process, the lower part of the box was moved with a constant rate of 0.3 mm/minute while the upper part was kept stationary. Three different normal stress levels, 23 kPa, 33.5 kPa and 55 kPa, were applied on top of the shear box. Details of the typical DE simulations of direct shear tests are provided elsewhere (Tran et al., 2014). Using a scale factor of 1, the grain size distribution used in the model follows the measured distribution of actual backfill material. It is noted that while the particle size distribution is considered realistic, the spherical-shaped particles and the contact model are somewhat artificial. As the behavior of discrete element assemblies depends not only on the microscopic parameters, but also on the particle shape, the grain size distribution and the contact model, three important microscopic parameters (friction angle, rolling resistance and contact stiffness) are varied to match the experimental results, as summarized in Table 2. Other parameters are identified as follows: the particle density is 2700 kg/m³ and the K_T/K_N ratio is fixed to be 0.25, as suggested by Tran et al. (2014).

3.3. Capturing the interaction effects

After the final particle assembly is formed, the geogrid and the pipe are allowed to freely deform. A strip footing (100 mm × 450 mm), similar to that used in the experiment, is simulated by gradually applying surface pressure using a displacement control scheme, as illustrated in Fig. 7. The input parameters are then assigned to the particles and the finite elements. A friction angle with a tangent value of 0.8 is applied between the footing and the DE particles to simulate the foundation base used in the experiment. No friction is used for the interface between the particles and the box walls. To examine the effect of the particle-interface interaction on the response of the footing model, a parametric study was conducted and the results revealed that the stiffness of the interface elements does not have a significant effect on the numerical results. It is noted that choosing unrealistically small stiffness values for the interface can cause the DE particles to deeply penetrate into the finite elements making it hard to bring it back to the DE domain. Contrarily, choosing unrealistically high interface stiffness values can lead to smaller critical time steps and this leads to an increase in computational costs. Therefore, the stiffness values of the interface elements are assigned to have the same values as the DE particles.

On the other hand, the coefficient of friction between the DE particles and the interface elements was found to affect the overall response of the soil-geogrid-pipe system. Therefore, the friction coefficient needs to be determined through a calibration process based on the experimental results. This friction coefficient compensates for the fact that spherical particles generally mobilize less frictional contact with structural surfaces as opposed to real sand particles. Therefore, a parametric study was performed to investigate the effect of the particle-interface friction coefficient on the overall system

response, from which a particle-interface coefficient with a friction of 0.45 was determined, as given in Table 2.

4. Results and Discussions

4.1. Load-displacement relationship

The relationships between the applied footing pressure and the surface displacement, with and without geogrid reinforcement, are shown in Fig. 9. The effect of adding a geogrid layer can be illustrated by comparing the measured responses for both the reinforced and the unreinforced cases. For a given surface displacement, a significant increase in the footing pressure was recorded with the use of geogrid reinforcement. It should be noted that the applied pressure was limited by the capacity of the tactile sensors (20 psi or 140 kPa); and therefore, the tests were stopped before the footing pressure reached the ultimate bearing capacity in both cases. The calculated soil responses are also plotted in the same figure for validation purposes. It can be seen that the numerical results agree well with the experimental data for both the reinforced and the unreinforced conditions.

4.2. Initial pressure distributions on the pipe

The measured and the calculated initial pressure levels acting on the pipe are shown in Fig. 10. For comparison purposes, the distributions of pressure for the cases of unreinforced and reinforced soils are presented on opposite sides of the polar chart. The use of tactile sensors allows for the distribution of pressure on the pipe to be continuously measured. Even though careful efforts were made to ensure the consistency of the initial pressure distributions for both the unreinforced and the reinforced cases, a

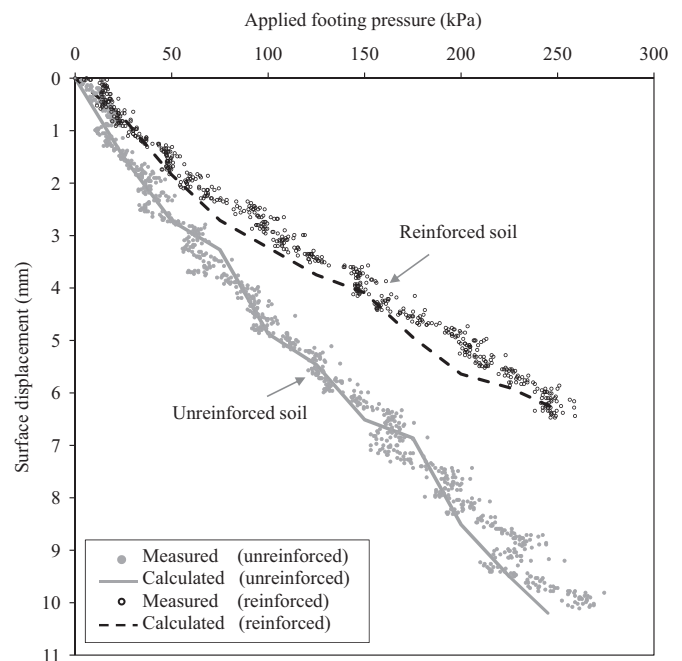


Fig. 9. Load-displacement relationship due to footing load over reinforced and unreinforced soil.

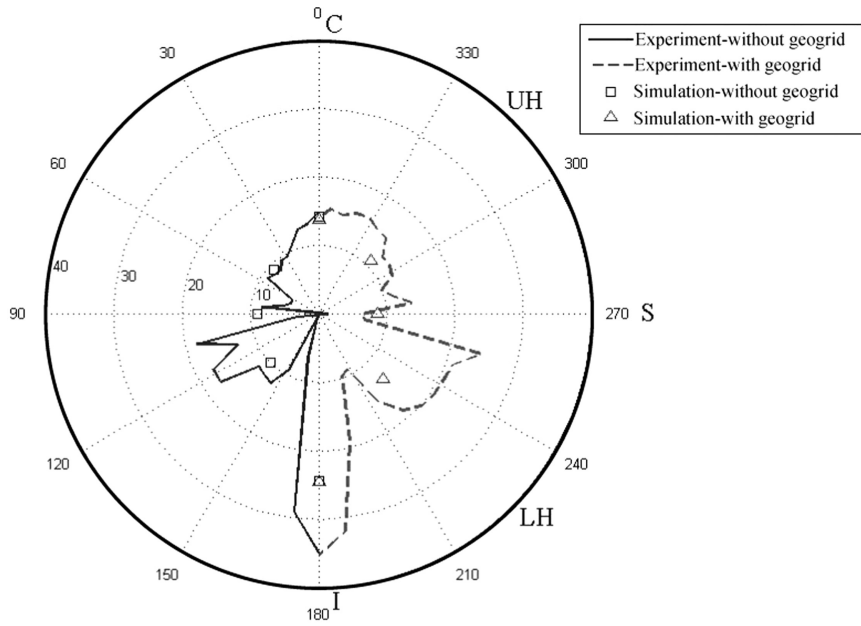


Fig. 10. Initial pressure distribution on pipe (units: kPa).

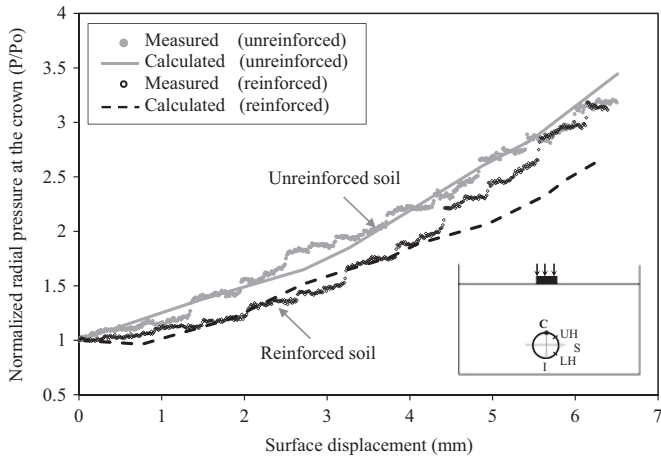


Fig. 11. Changes in radial pressure at crown.

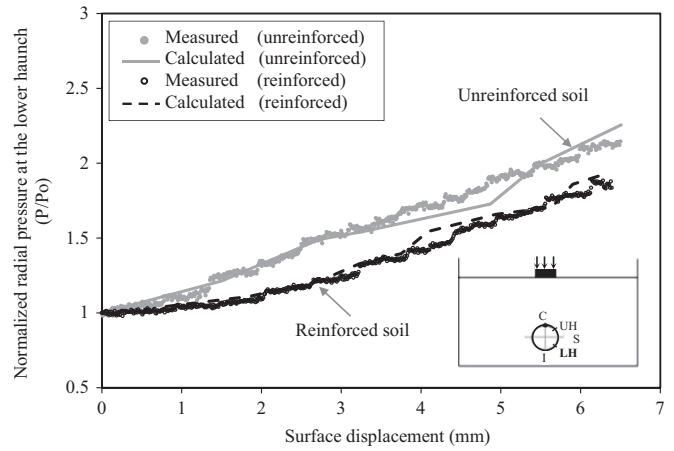


Fig. 13. Changes in radial pressure at lower haunch.

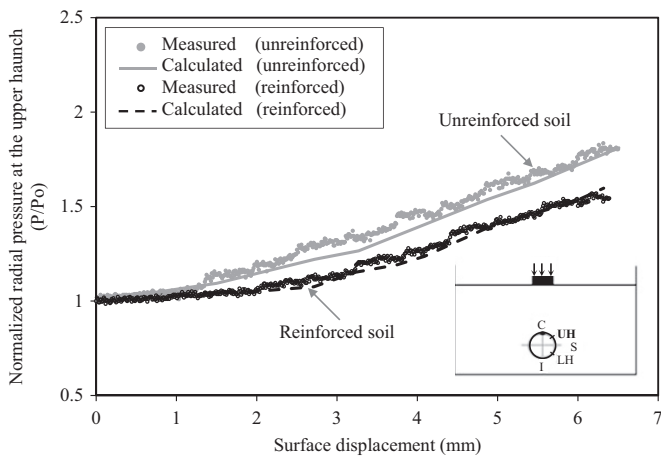


Fig. 12. Changes in radial pressure at upper haunch.

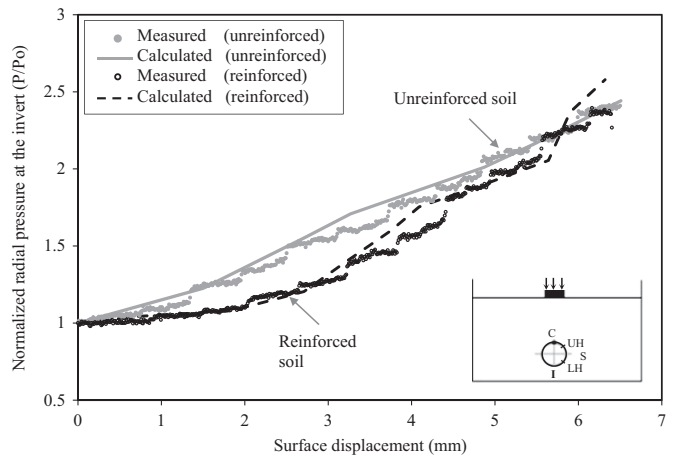


Fig. 14. Changes in radial pressure at invert.

small difference in pressure was observed in the experimental results for the two cases, as illustrated in Fig. 10. This difference can be explained by the possible variation in tamping forces during the soil placement process. The use of tactile sensors allowed for small changes in pressure to be continuously recorded around the pipe. The largest radial pressure values were observed at the pipe invert. The calculated pressure at this location was found to depend on the damping forces applied during the particle generation process. Although general agreement between the experimental and the numerical results is observed, Fig. 10 shows that smaller radial pressures were calculated near the springline as compared to the measured values. This may be attributed to the fact that two sensing pads were connected around this location leading to a slight change in the pressure readings.

4.3. Increase in pressure on the pipe due to applied footing load

The changes in radial pressure acting on the pipe during the loading process are analyzed and compared with the measured values. Four locations have been chosen to investigate the

pressure changes including the pipe crown, the upper haunch, the lower haunch and the invert. The springline of the pipe was not selected for the analysis due to the significant difference between the measured and the calculated values at this location. The changes in pressure at the crown, the upper haunch, the lower haunch and the invert are presented in Figs. 11–14, respectively. In each figure, the normalized radial pressure is presented against the surface displacement below the footing for the unreinforced and reinforced cases. It can be seen from Figs. 11 through 14 that the radial pressure acting on the pipe generally increased with the increase in footing pressure. At an applied displacement of 6.5 mm, the increase in pressure around the pipe was found to be the highest at the crown (Fig. 11), followed by the invert (Fig. 12) and then by the upper and lower haunches (Figs. 13 and 14). The presence of the geogrid layer resulted in a decrease in the radial pressure, particularly at high displacement levels. This can be explained by the mobilization of the geogrid strength as part of the vertical load is transferred laterally through the geogrid material. This illustrates the possible usefulness of the geogrid in reducing the effect of surface loading on buried pipes. By

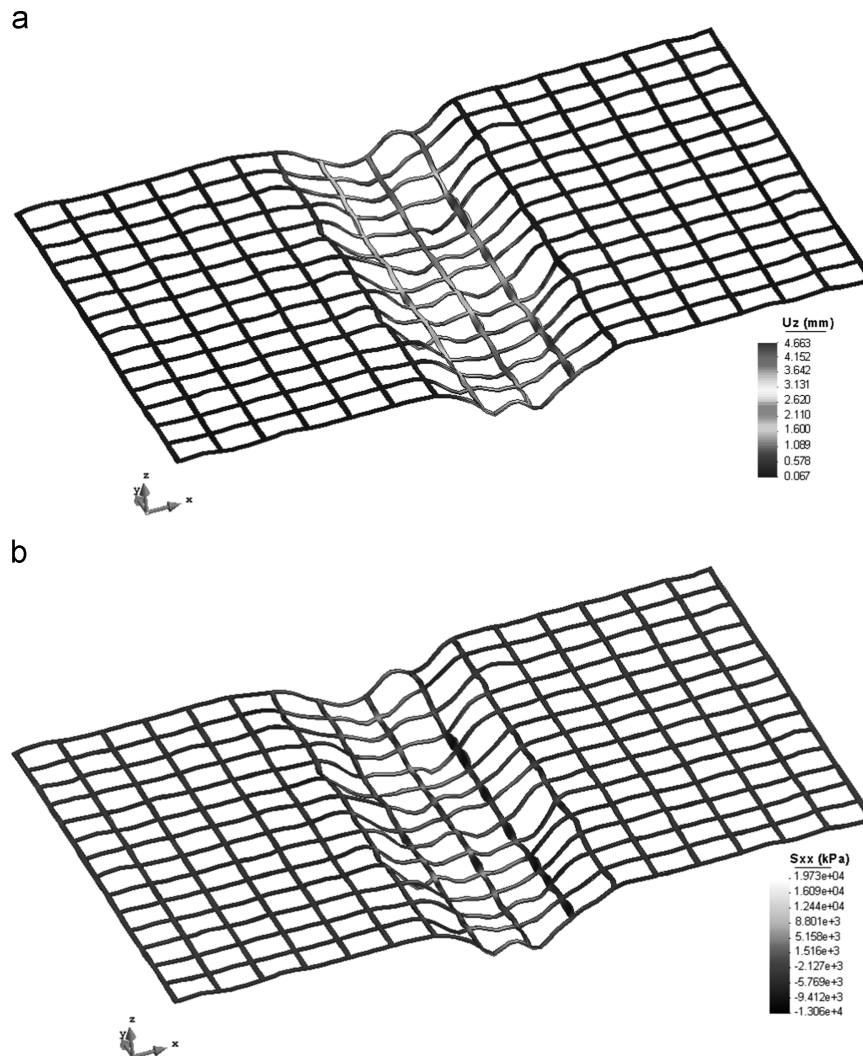


Fig. 15. Geogrid response at footing pressure of 200 kPa: a) vertical displacement and b) Geogrid stress (S_{xx}).

comparing the experimental and numerical results, it can be seen that the coupled finite-discrete element method was able to essentially capture the radial pressure distribution on the pipe.

4.4. Behavior of the geogrid

The vertical displacement of the geogrid and the induced tensile stress (S_{xx}) at an applied footing pressure of 200 kPa are shown in Fig. 15a and b, respectively. It can be seen that the deformation of the geogrid occurred mainly in a region located directly below the footing. Very small deformations were calculated outside this region. Stress S_{xx} was found to be high below the footing and then decreased with distance away from the loaded area. The numerically calculated geogrid deformation pattern is consistent with that observed during the experiments.

4.5. Effect of geogrid reinforcement on radial pressure at high surface loads

Since the experiments had to be terminated prior to reaching a complete soil failure under the applied footing pressure, additional numerical modeling was performed by progressively increasing the applied load and recording the corresponding changes in radial pressure on the pipe for the reinforced and unreinforced cases. This is deemed necessary to fully

investigate the efficiency of the geogrid at higher strain levels. It has been shown from Figs. 11 through 14 that up to a vertical displacement of about 6.5 mm, the effect of the geogrid in reducing the induced pressure on the pipe was highest at the crown and much less at the upper haunch. The changes in radial pressure at these two locations, due to the additional increase in surface loading up to the ultimate soil bearing capacity, are shown in Fig. 16a and b, respectively. It can be seen that the efficiency of the geogrid in reducing the radial pressure on the pipe increased with an increase in the footing load. This is explained by the increase in interlocking resistance between the geogrid and the backfill as a result of the additional induced geogrid deformation leading to less vertical pressure transmitting down to the pipe.

5. Summary and Conclusions

This study has investigated the distribution of earth pressure on buried pipes using both experimental work and numerical analysis. The contact pressure distribution on a rigid pipe was measured using tactile sensing technology. The buried pipe was installed in gravel backfill material and subjected to strip surface loading. The tactile sensors provided a continuous pressure profile around the pipe. The effect of installing a layer of geogrid reinforcement near the surface on the radial pressure distribution on the pipe was examined. A multi-scale finite-discrete element framework was used to investigate both the soil-pipe and the soil-geogrid interactions.

The contact pressure obtained using the performed numerical analysis was found to be in agreement with the experimental results. Radial pressure acting on the pipe generally increased with an increase in the applied footing load. With the introduction of geogrid reinforcement, the radial pressure acting on the pipe was found to be smaller than that of the unreinforced case. This indicates that the effect of the geogrid increased with the increase in surface loading.

Finally, the finite-discrete element approach, presented in this study, has proven to be effective in capturing the response of both the pipe and the geogrid and their interaction with the surrounding ground.

Acknowledgements

This research was supported by a research grant from the Natural Sciences and Engineering Research Council of Canada (NSERC). The authors would also like to gratefully acknowledge the support of Dr. W.D. Cook and Mr. J. Bartczak for conducting these experiments.

References

- Abu-Farsakh, M., Chen, Q., Sharma, R., 2013. An experimental evaluation of the behavior of footings on geosynthetic-reinforced sand, *Soils and Foundations*, 53(2), 335-348.
- Ahmed, M.R., Meguid, M.A., 2009. The effect of subsurface volume loss on the bearing capacity of reinforced granular material. 62nd Can. Geotech. Conf., Halifax, CD, 6 pages.

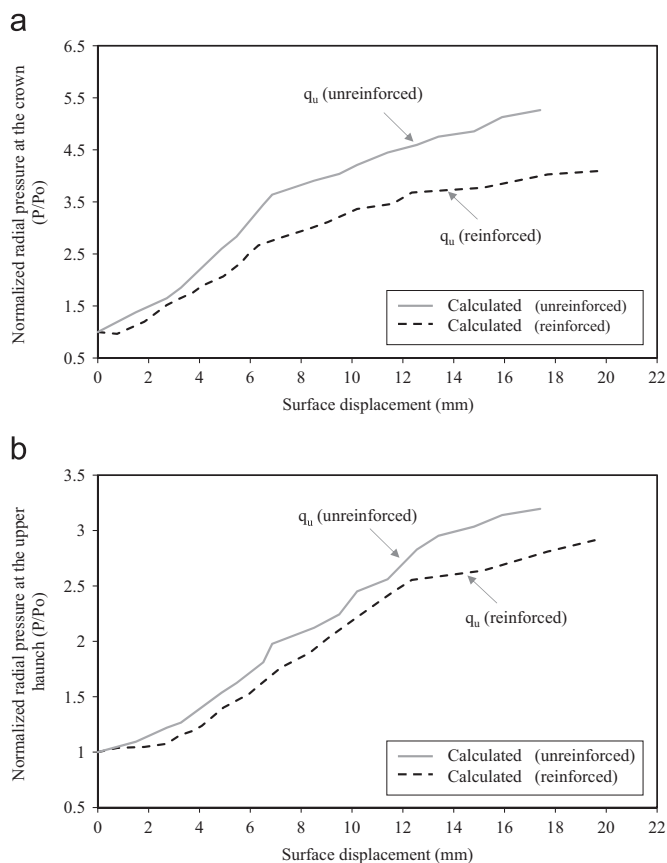


Fig. 16. Changes in radial pressure up to soil failure: a) at crown and b) at upper haunch.

- Ahmed, M.R., Meguid, M.A., Whalen, J., 2013. Laboratory Measurement of the Load Reduction on Buried Structures overlain by EPS Geofoam. 66th Can. Geotech. Conf., Montreal, CD, 8 pages.
- Carlson, R.W., 1939. Development and analysis of a device for measuring compressive stress in concrete. UN-11-M. Massachusetts Institute of Technology PhD Thesis.
- Chakraborty, M., Kumar, J., 2014. Bearing capacity of circular foundations reinforced with geogrid sheets. *Soils and Foundations* 54 (4), 820–832.
- Corey, R., Han, J., Khatri, D.K., Parsons, R.L., 2014. Laboratory study on geosynthetic protection of buried steel-reinforced HDPE pipes from static loading. *Journal of Geotechnical and Geoenvironmental Engineering*. 140 (6), 401–419.
- Dang, H.K., Meguid, M.A., 2010. Evaluating the performance of an explicit dynamic relaxation technique in analyzing nonlinear geotechnical engineering problems. *Computers and Geotechnics* 37 (1), 125–131.
- Dang, H.K., Meguid, M.A., 2013. An efficient finite-discrete element method for quasi-static nonlinear soil-structure interaction problems. *International Journal for Numerical and Analytical Methods in Geomechanics* 37 (2), 130–149.
- Dunnicliff, J., Green, G.E., 1988. *Geotechnical instrumentation for monitoring field performance*. Wiley, New York.
- Gillis, K.M., 2013. Tactile pressure sensor calibration methods and data analysis for geotechnical centrifuge modeling. University of Colorado at Boulder, 75 M.E. Thesis.
- Hanna, T.H., 1985. *Field instrumentation in geotechnical engineering*. Trans Tech Publications.
- Kohl, K.M., New, B.M., O'Rourke, T.D., 1989. Stress cell measurements for the investigation of soil pipeline interactions during vehicular loading. Proc., *Geotechnical Instrumentation in Civil Engineering Projects*. Univ. of Nottingham, Nottingham, U.K.
- Lazebnik, G.E., Tsinker, G.P., 1997. *Monitoring of soil-structure interaction: instruments for measuring soil pressures*, 1st Edition Springer.
- Olson, S.M., Hashash, Y., Polito, C., Phillips, C., Muszynski, M., 2011. Measuring Pressures in the Geotechnical Centrifuge using Tactile Pressure Pads, 7th Annual NEES Centrifuge Research and Training Workshop Rensselaer Polytechnic Institute.
- Paikowsky, S.G., Hajduk, E.L., 1997. Calibration and use of grid-based tactile pressure sensors in granular material. *Geotech. Test. J* 20 (2), 218–241.
- Paikowsky, S.G., Palmer, C.J., Dimillio, A., 2000. Visual observation and measurement of aerial stress distribution under a rigid strip footing. *Geotechnical Special Publication* 94, 148–169.
- Paikowsky, S.G., Tien, H.S., 2002. Experimental examination of the arching mechanism on the micro level. *Geotechnical Special Publication* 117, 222–228.
- Paikowsky, S.G., Palmer, C.J., Rolwes, L.E., 2006. The Use of Tactile Sensor Technology for Measuring Soil Stress Distribution. *Geotechnical Engineering in the Information Technology Age ASCE GeoCongress*, Atlanta, Georgia, 1–6.
- Palmer, M.C., O'Rourke, T.D., Olson, N.A., Abdoun, T., Ha, D., O'Rourke, M.J., 2009. Tactile Pressure Sensors for Soil-Structure Interaction Assessment. *Journal of Geotechnical and Geoenvironmental Engineering* 135 (11), 1638–1645.
- Peattie, K.R., Sparrow, R.W., 1954. The fundamental action of earth pressure cells. *Journal of the Mech. and Phys. of Solids* 2, 141–145.
- Pressure Profile Systems, Tactarray distributed pressure measurement system: (<http://www.pressureprofile.com/tact-array-sensors/>).
- Selig, E.T., 1964. A review of stress and strain measurement in soil. *Proceedings of the Symposium on Soil-Structure Interaction*. University of Arizona, 1964.
- Šmilauer, V., Chareyre, B., 2010. Yade dem formulation. In *Yade Documentation* (V. Šmilauer, ed.), The Yade Project, 1st ed. (<http://yade-dem.org/doc/formulation.html>).
- Springman, S.M., Nater, P., Chikatamarla, R., Laue, J., 2002. Use of flexible tactile pressure sensors in geotechnical centrifuge. Proc. Of the Int. Conference of Physical Modeling in Geotechnical Engineering, 113–118.
- Talesnick, M., 2005. Measuring soil contact pressure on a solid boundary and quantifying soil arching. *ASTM J. Geotech. Test* 28 (2), 171–179.
- Talesnick, M.L., Xia, H.W., Moore, I.D., 2011. Earth pressure measurements on buried HDPE pipe. *Geotechnique* 61 (9), 721–732.
- Tessari, A., Sasanakul, I., Abdoun, T., 2010. Advanced sensing in geotechnical centrifuge models. 7th International Conference on Physical Modelling in Geotechnics, 395–400.
- Tran, V.D.H., Meguid, M.A., Chouinard, L.E., 2013. A Finite-Discrete Element Framework for the 3D Modeling of Geogrid-Soil Interaction under Pullout Loading Conditions. *Geotextiles and Geomembranes* 37, 1–9.
- Tran, V.D.H., Meguid, M.A., Chouinard, L.E., 2014. Discrete Element and Experimental Investigations of the Earth Pressure Distribution on Cylindrical Shafts. *International Journal of Geomechanics* 14 (1), 80–91.